PAPER

Advancing semiconductor–electrocatalyst systems: application of surface transformation films and nanosphere lithography

Katharina Brinkert, [iD] *[a] Matthias H. Richter,[ac] Ömer Akay,[d] Michael Giersig,[d] Katherine T. Fountaine[ef] and Hans-Joachim Lewerenz[b]

Photoelectrochemical (PEC) cells offer the possibility of carbon-neutral solar fuel production through artificial photosynthesis. The pursued design involves technologically advanced III–V semiconductor absorbers coupled *via* an interfacial film to an electrocatalyst layer. These systems have been prepared by *in situ* surface transformations in electrochemical environments. High activity nanostructured electrocatalysts are required for an efficiently operating cell, optimized in their optical and electrical properties. We demonstrate that shadow nanosphere lithography (SNL) is an auspicious tool to systematically create three-dimensional electrocatalyst nanostructures on the semiconductor photoelectrode through controlling their morphology and optical properties. First results are demonstrated by means of the photoelectrochemical production of hydrogen on p-type InP photocathodes where hitherto applied photoelectrodeposition and SNL-deposited Rh electrocatalysts are compared based on their *J–V* and spectroscopic behavior. We show that smaller polystyrene particle masks achieve higher defect nanostructures of rhodium on the photoelectrode which leads to a higher catalytic activity and larger short circuit currents. Structural analyses including HRSEM and the analysis of the photoelectrode surface composition by using photoelectron spectroscopy support and complement the photoelectrochemical observations. The optical performance is further compared

[a]Division of Chemistry and Chemical Engineering, California Institute of Technology, 1200 E California Blvd, Pasadena, CA 91125, USA. E-mail: brinkert@caltech.edu

[b]Division of Engineering and Applied Science, Joint Center for Artificial Photosynthesis, California Institute of Technology, 1200 E. California Blvd, Pasadena, CA 91125, USA

[c]Brandenburg University of Technology Cottbus, Applied Physics and Sensors, K.-Wachsmann-Allee 17, 03046 Cottbus, Germany

[d]Freie University Berlin, Arnimallee 14, 14195 Berlin, Germany

[e]Resnick Sustainability Institute, California Institute of Technology, Pasadena, California 91125, USA

[f]Northrop Grumman Corporation, NG Next Nanophotonics & Plasmonics Laboratory, Redondo Beach, California 90278, USA

to theoretical models of the nanostructured photoelectrodes on light scattering and propagation.

1   Introduction

Rapid changes in the global climate during the last century and the quest for sustainable and efficient energy conversion systems have guided research in the past decades towards the development of biomimetic, artificial photosynthesis systems. The more efficient systems follow the concept of the Z-scheme of natural photosynthesis.[1,2] Current research avenues comprise the use of semiconductors with sufficiently large energy gaps for unassisted water splitting,[3] surface functionalized tandem photovoltaic structures[4–6] and hybrid Earth abundant – technologically advanced light absorbers.[7,8] Each approach has its advantages: single junction water splitting is technologically rather simple as the system is based on a single absorber only. Tandem cells show the highest solar-to-hydrogen (STH) efficiency and the hybrid structures incorporate more Earth abundant materials. On the basis of theoretical considerations of the absolute limits in light-induced unassisted water splitting in a monolithic device,[9] it is of considerable interest to experimentally realize high STH efficiencies. In surface functionalized tandem solar cells, however, issues are stability, catalyst activity and its optical attenuation. The present benchmarking devices are based on III–V semiconductors with dual junctions.

The introduction of corrosion protection films to these combined semiconductor–electrocatalyst systems knows three routes: (i) the use of insoluble (photo)corrosion layers typically achieved by potential cycling under well-defined conditions,[4,10] (ii) atomic layer deposition (ALD) of films with a large energy gap that are optically transparent and can also function as antireflection layers[6,11] and (iii) the incorporation of a larger energy gap photocatalyst material as the surface terminating layer that is electronically connected to the underlying absorber system.[12]

Here, we pursue the first route and generate an interfacial stabilization film through *in situ* conditioning of a single crystalline p-InP, (111)A oriented surface, but focus on advancing the hitherto empirical electrocatalyst deposition routines. Typical catalyst preparation uses sputtering, evaporation and e-beam lithography.[13–15] We employ and study an approach to obtain well-defined desired catalyst nanostructures of high fidelity, provided by shadow nanosphere lithography (SNL).[16]

Shadow nanosphere lithography utilizes the self-assembly of latex nanospheres for the creation of a colloidal monolayer, serving as a mask during the deposition process of materials. Modification of the mask and changes in the materials' deposition process allow the creation of various nanopatterns. Hitherto, SNL has been used as a time-efficient and low-cost lithographic method to produce large arrays of nanostructures exhibiting interesting optical responses, which make them susceptive to a variety of applications in optoelectronics, optical lithography and biotechnology.[17–19]

Here, SNL is utilized to prepare distinct electrocatalyst nanostructures for optimizing the optoelectronic and catalytic properties of photodiode–electrocatalyst systems for light-induced hydrogen production. p-type InP, which is one

of the most efficient photocathode materials for hydrogen evolution,[10,20] is used as the photoactive semiconductor. As an efficient electrocatalyst,[21] we use rhodium which is characterized by a high exchange current density. Its optical properties depend on the size of the prepared nanoparticles, condensed into a rather continuous film.[6] We compare the J–V characteristics and the spectroscopic behaviour of photoelectrodes where Rh is photoelectrodeposited from a Rh(III) solution onto the semiconductor to photocathodes, where Rh is photo-electrodeposited onto the semiconductor through differently sized polystyrene particle masks provided by the SNL technique. Our findings indicate that the designed electrocatalyst nanostructures provide significant advantages over the direct deposit "thin-film" structure for the photoelectrocatalytical half-cell performance. These advantages are assigned to changes in the improved catalytic properties of the nanostructured electrocatalyst and its optical properties.

2 Experimental

2.1 Preparation of p-InP photoelectrodes

(111)A-oriented single crystal p-InP wafers from AXT Inc. (Geo Semiconductor Ltd. Switzerland) were used with a Zn doping concentration of 5×10^{17} cm^{-3}. The ohmic back contact was made by evaporating 4 nm Au, 80 nm Zn and 150 nm Au and heating to 400 °C for 60 s. Before photoelectrochemical conditioning, the 0.5 cm^2 polished (111)A indium face of p-InP was etched for 30 s in bromine (0.05% (w/v))/methanol solution followed by rinsing with ethanol and ultrapure water and drying under nitrogen flux. Solutions were made from ultrapure water with an organic impurity level below 50 ppb and from analytical grade chemicals. Current–voltage and chronoamperometric measurements were performed in a standard three-electrode potentiostatic arrangement. For the subsequent photoelectrochemical conditioning, a carbon electrode was used as the counter electrode and Ag/AgCl (3 M) was taken as the reference electrode. All potentials are converted to RHE. During photoelectrochemical conditioning in 0.5 M HCl, the solutions were purged with nitrogen of 5.0 purity. The surface conditioning was realized by potentiodynamic cycling under illumination (100 mW cm^{-2}) between −0.44 V and +0.31 V at a scan rate of 50 mV s^{-1}. For illumination, a white-light 1000 W mercury–xenon arc lamp with a calibrated AAA grade AM 1.5G filter was used. The light intensity was set to 100 mW cm^{-2} using a calibrated silicon reference solar cell. The samples were rinsed with MiliQ water and dried under N$_2$.

Rhodium was photoelectrochemically deposited from a solution of 5 mM RhCl$_3$, 0.5 M NaCl and 0.5% (v/v) 2-propanol for 3 s at a constant potential of $V_{dep} = +0.01$ V during white-light illumination (100 mW cm^{-2} as described above), resulting in the formation of a thin film or a nanostructured surface morphology if deposited through a polystyrene mask (see below).

2.2 Fabrication of rhodium nanostructures

The rhodium nanostructures on the InP substrate were fabricated using shadow nanosphere lithography (SNL, Fig. 1).[16] Polystyrene beads with the sizes 260 nm, 789 nm and 1400 nm were obtained at a concentration of 5% (w/v) from micro-particles GmbH. For creating the masks, mono-dispersed beads of polystyrene (PS) were dissolved in MiliQ water and further diluted. In order to obtain 600 µl of
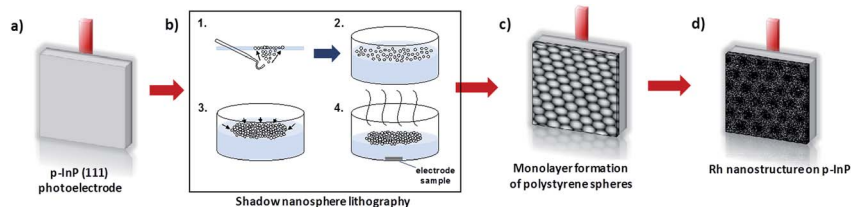
Fig. 1 Scheme of the Rh nanoparticle preparation on p-InP photoelectrodes *via* shadow nanosphere lithography. (a) The p-InP electrode is photoelectrochemically conditioned (see text for details). In parallel, a closely-packed mask of polystyrene spheres is prepared in a Petri dish (see box, (b)): (1) deposition of polystyrene spheres (PS) on the water surface; (2) self-assembly and (3) close-packing of PS spheres; (4) deployment of close packed spheres on InP electrode by water evaporation. (c) Tapping mode AFM image of the InP surface with a monolayer of 789 nm polystyrene particles. (d) HRSEM image of Rh nanostructure after photoelectrochemical deposition of Rh and removal of 789 nm PS spheres.

the final solution, 300 μl of the PS-beads dispersion was mixed with 300 μl of ethanol containing 1% (w/v) styrene and 0.1% sulphuric acid (w/v). The prepared solution was finally applied onto the air–water interface using a Pasteur pipette with a curved tip. To further raise the area of the monocrystalline structures, multiple smaller domains were transformed into larger ones by gently turning the Petri dish. The amount of solution was distributed to cover 50% of the water surface with a hcp monolayer, leaving some place for stress relaxation and to avoid formation of cracks in the lattice during the next steps of the preparation. The photoelectrochemically conditioned p-InP electrodes are placed delicately into the Petri dish under the floating closed packed PS sphere mask. After removing most of the water by pumping and letting the residual water evaporate, the mask deposits onto the electrode. After drying the surface with N_2, Rh was deposited through the PS spheres as described above. The samples were rinsed with MiliQ water and dried with a gentle flow of N_2. The PS-spheres were washed off the surface by placing them for 20 min under gentle stirring in a beaker with toluene. The electrodes were further cleaned by rinsing with acetone and ethanol. To remove residual carbon compounds from the surface, an O_2-plasma was used for 6 min at a process pressure of 0.16 mbar, a power of 65 W and gas inflows of O_2 and Ar of 2 sccm and 1 sccm, respectively.

2.3 Photoelectrochemical measurements

Photoelectro-chemical measurements were performed using a Biologic SP-200 potentiostat. 1 M $HClO_4$ was used as the electrolyte which was purged with N_2 (5.0 N) for a minimum of 20 min before usage. A saturated calomel electrode (SCE) was used as the reference electrode in the three-electrode measurement set-up. Borosilicate glass cells with a quartz window were used as the vessel for the experiments allowing them to be easily cleaned in Nochromix® solution. The carbon counter electrode was placed in close vicinity to the working electrode. *J–V* measurements were performed with a scan velocity of 50 mV s^{-1}. The same illumination conditions were used as for the photoelectrochemical conditioning (see above).

2.4 Structural and optical characterization

Optical measurements were performed to obtain reflectivity spectra of the thin-film and nanostructured photoelectrodes in air. A Cary 5000 UV/vis/NIR instrument with an integrating sphere that includes the measurement of the diffuse reflectivity was used. Scanning electron microscopy images were obtained with an FEI Nova NanoSEM 450 microscope. Tapping Mode Atomic Force Microscopy (TM-AFM, Bruker) was employed for the characterization of the surface morphology after deposition of the PS spheres to confirm monolayer coverage. The ScanAsyst mode was used to optimize the tapping (mode) frequency and other experimental parameters such as the gain, set point, and cantilever tuning. ScanAsyst-Air tips (silicon nitride) were used, with a nominal tip radius of 2 nm and a rotated (symmetric) geometry.

2.5 Photoelectron spectroscopy

X-ray Photoelectron Spectroscopy (XPS) was performed using a Kratos Axis Ultra and Surface Science M-Probe system with a base pressure of $<1 \times 10^{-9}$ mTorr. A monochromatic Al Kα source (hK = 1486.69 eV) with a power of 150 W was used for all measurements.

2.6 Computational simulations

Theoretical modelling of the optoelectronic performance of the thin film and nanostructured photoelectrodes was carried out using Lumerical FDTD, a commercial electromagnetic simulation software package. For the nano-structured electrodes, the patterns assumed were hexagonally close-packed polystyrene spheres; each sphere resulted in a truncated cone opening in the Rh layer with a lower radius corresponding to half of the polystyrene sphere radius and an upper radius that is 200 nm larger than the lower radius. The catalyst exchange current density is assumed to be 0.1 mA cm^{-2} ($j_{0,\text{cat}}$) corresponding to the known activity of Rh electrocatalysts. The dark current for the InP|Rh Schottky junction (j_0) is assumed to be 10^{-8} mA cm^{-2}; this value is based on a fit to the experimentally-measured current–voltage curves since the ideal equations for the dark current of a Schottky junction did not accurately describe the system, which is expected to be due to the interfacial InP$_x$O$_y$ layer. The f_{SA} value is 0.77 for the nanostructured electrodes and is calculated based on the optical model rendering of the structure described above. The previously considered series resistance in eqn (2)[9] was neglected in the description of the current–voltage behaviour of this system due to the fact that this experimental parameter influenced by a variety of variables only operates as an additional fitting parameter.

3 Results and discussion

3.1 Photoelectrochemistry

The behaviour of photoelectrochemical systems consists of the generation of excess electron–hole pairs through semiconductor light absorption, the separation of excess carriers and the electrochemical reaction at the catalyst–solution interface. The degree to which these photodiode–electrocatalyst systems are electrocatalytically limited depends on the exchange current density and Tafel

slope of the electrocatalyst, the fill factor of the photodiode and the total device current.[11–13] Regarding the overall efficiency, electrocatalyst characteristics, demonstrating large exchange current densities and small Tafel slopes are among other characteristics crucial parameters of the optimization process.

The current–voltage characteristics of the conditioned nanostructured and thin film photoelectrodes (Fig. 2), were measured in 1 M HClO$_4$ in the dark and under white light illumination. Fig. 2 shows the obtained dark- (a) and photo-currents (b) of the electrodes with applied voltage. The dark currents indicate distinct differences: the thin film photoelectrode demonstrates an increased anodic dark current, whereas the nanostructured electrode resulting from the Rh deposition through polystyrene particles exhibited a better blocking behaviour in the anodic region. These differences translate directly to the light-induced currents: the nanostructured photoelectrodes showed a significant photocurrent increase in comparison to the thin film sample, with a short circuit current being increased by about 10 mA cm^{-2} for the samples with the smallest polystyrene particle size (260 nm). The application of larger polystyrene particles led also to an increased photocurrent density, whereas the fill factors of the 789 nm and 1400 nm samples were about 20% lower than the ones obtained from the thin film photoelectrode and for the 260 nm particle size one.

The experimental observations were related to a theoretical model on the coupled optoelectronic performance of these devices which is based on a semi-analytic formalism for PEC devices with nanostructured catalysts developed in previous publications.[9,22,23] The InP absorption spectrum (f_A) was obtained by applying a transmission monitor below the Rh layer to determine the absorption in the InP. This was further on weighed with the AM 1.5G spectrum and integrated to obtain the absorbed photocurrent, j_L, according to eqn (1), in which λ is the wavelength and λ_{E_g} is the wavelength corresponding to the semiconductor band edge (925 nm for InP):

$$j_L = \int_0^{\lambda_{E_g}} f_A(\lambda) \text{AM } 1.5G(\lambda) d\lambda \tag{1}$$

The device structure is defined in the optical simulations as a semi-infinite layer of InP coated with an 8 nm layer of InP$_x$O$_y$ and an 8 nm effective medium
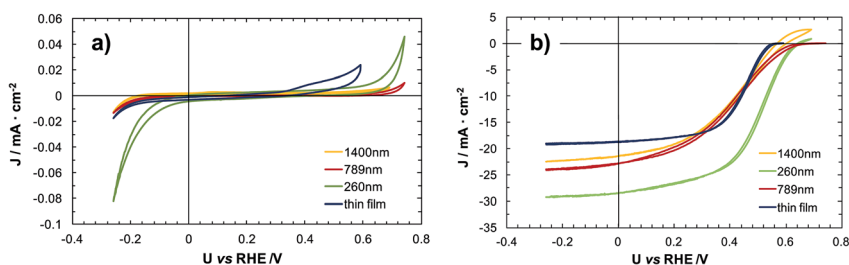

Fig. 2 $J-V$ measurements of the nanostructured and thin-film p-InP–Rh photocathodes in 1 M HClO$_4$. The size of the applied polystyrene particle spheres on the p-InP surface prior to Rh deposition is indicated in the legend. (a) Dark and (b) photocurrent measurements under simulated AM 1.5G conditions. The scan rate was set to 50 mV s^{-1} and the measurements started at the open circuit potential.

layer of Rh, all embedded in water. These structure assumptions are based on a previous publication.[24] The optics of the Rh|H$_2$O effective medium layer were calculated using the Maxwell Garnett approximation[25] with a 0.4 fill fraction of Rh. The current–voltage behaviour of the device is captured via eqn (2), an analytic equation for the current–voltage behaviour of the nanostructured PEC device[22] which is essentially the difference between the photovoltage of the diode (V_{PV}) and the overpotential of the catalyst (η_{cat}).

$$V_{PEC}(j) = \frac{kT}{q} \ln\left(\frac{j_L - j}{j_0} + 1\right) - \frac{2RT}{n_e F} \sin h^{-1}\left(\frac{j}{2j_{0,cat}f_{SA}}\right) \qquad (2)$$

here, $j_{0,cat}$ is the catalyst exchange current density, j_0 is the dark current for the InP|Rh Schottky junction and f_{SA} is a parameter normalizing the catalyst surface area to the planar device area.[9]

The nanostructured patterns assume the hexagonal close-packing of the PS spheres. In addition, each sphere resulted in a truncated cone as mentioned above in the methods section and as shown in the insert of Fig. 3. Fig. 3a shows the calculated J–V curve of the nanostructured photoelectrode onto which Rh was deposited for PS spheres of 260 nm. The inset in the left corner illustrates the used InP–Rh modelling structure. The simulated J–V characteristic matches the experimentally obtained J–V behaviour in Fig. 1b very well, although for the larger particle sizes, the simulations predicted higher short circuit currents as demonstrated in Fig. 3b. This could be caused by the applied model structure, which uses a continuous Rh layer with larger holes and the nanostructure of the single Rh catalyst that makes up the overall topography (see Fig. 5) is not fully accounted for. Furthermore, non-idealities in the diode are not considered in this model. However, the model allows the reproduction of the photocurrent–voltage behaviour and the trends observed for the various PS sphere sizes.

3.2 Optical characterization

In order to comprehend the differences in the photoelectrocatalytical behaviour, the optical and electronic properties of the nanostructured and thin film
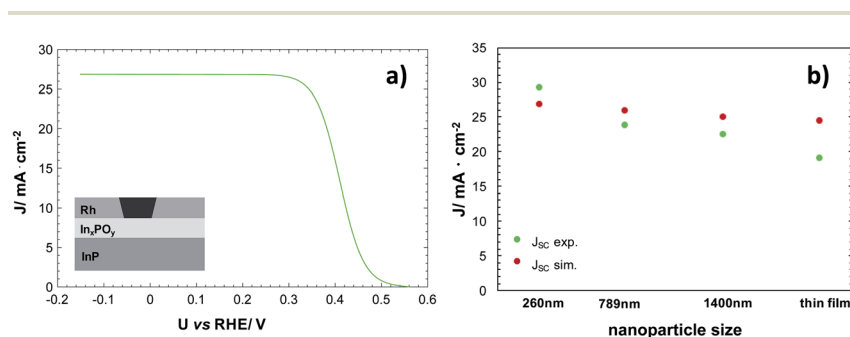

Fig. 3 (a) Modelled J–V measurements of the nanostructured p-InP–Rh photocathode under simulated AM 1.5G conditions in 1 M HClO$_4$ using polystyrene spheres of 260 nm. The inset in the left corner illustrates the applied modelling structure of the system (see text for details). (b) Calculated and experimentally observed short circuit currents (at $U = 0$ V) for the different nanoparticle sizes.

photoelectrodes were investigated and compared. Fig. 4 shows the simulated and experimentally obtained reflectivity of the nanostructured and thin film photoelectrodes. The sample with the inhomogeneous surface morphology (PS particle size 260 nm) shows about 10% less reflectance than the sample with a PS sphere size of 1400 nm and the thin film electrode, indicating an effective optically almost transparent nanostructured metallic catalyst layer. This lower reflectivity contributes to the observed significantly improved photocurrent–voltage behaviour. Although, here, too, the trend of the experimental data displayed in Fig. 4b and c is reproduced where the thin film and the 1400 nm PS samples show the highest reflectivity, the experimental data show larger individual differences. This also relates to the integrated absorption that is displayed in Fig. 4d. Interestingly, when comparing the experimentally determined normalized absorption (c) with the measured normalized short circuit photocurrent (d), a parallel trend with the PS sphere radii is shown, except for the thin film sample.

Also, the deviations in j_{SC} are considerably larger than those in absorption, pointing to a major influence of the catalyst deposits on the semiconductor/interphase film/Rh junction and its electronic properties. This, in turn, explains why purely optical modelling does only partially account for the observed photoelectrocatalytic behaviour. In addition, the presently employed optical model can be advanced to closer approach the realistic situation. This is work in progress where cross sectional TEM data will be needed. The absorption spectra for each of the devices demonstrate clearly, however, that the nanostructured photoelectrodes outperform the thin film one due to the improved coupling of light
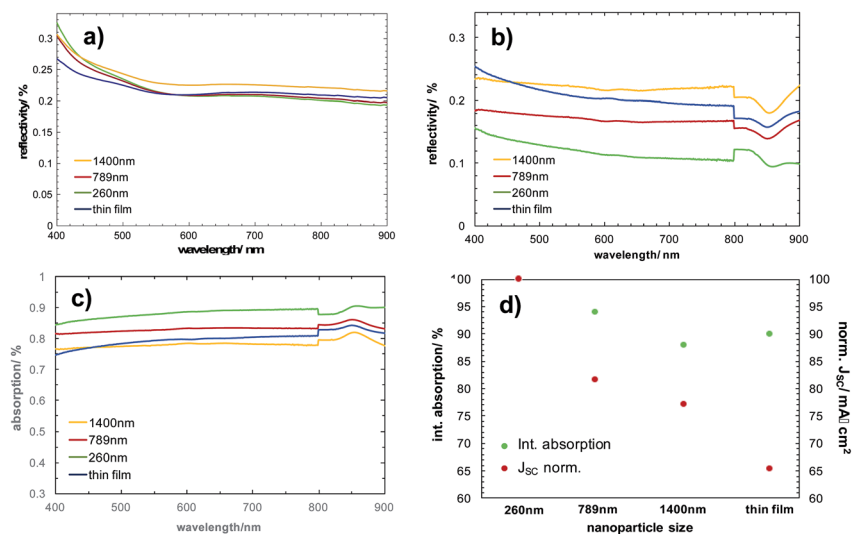

Fig. 4 (a) Calculated reflectance spectrum of the thin film and nanostructured p-InP–Rh electrodes. (b) Experimentally obtained reflectance spectrum of the photoelectrodes. (c) Absorption measurements of the nanostructured and thin-film p-InP–Rh photocathodes. (d) Integrated absorption of the electrodes in comparison to the normalized short circuit photocurrents of the different systems. In both cases, the 260 nm sample corresponds to 100%. The applied polystyrene particle sizes prior to Rh electrodeposition are indicated in the legend.

into the InP; additionally, the smaller particle designs exhibit the best optical performance. This trend agrees well with the trend of experimentally-measured short circuit currents.

3.3 Surface topography and chemistry

Fig. 5 shows HRSEM images of the electrode surface topographies after PS sphere removal and Rh deposition. Differences in the surface morphology of the photoelectrodes are clearly visible: the application of smaller polystyrene beads (260 nm) leads to an inhomogeneous pattern of holes, whereas a large area of defect-free arrays of holes becomes visible when PS spheres of 789 nm and 1400 nm are used. Both nanostructures exhibit a high quality long-range order and can be clearly distinguished from the thin film electrode. Although the same electrode-position conditions were applied for all samples, distinct differences are seen in the deposited Rh particle size and the arrangement of the nanoparticle conglomerate as indicated in Table 1. Larger rhodium particles were observed on samples with 789 nm and 1400 nm PS spheres, whereas their size is homogeneously smaller on samples when 260 nm PS spheres were applied.

The determination of the photoelectrodeposition dynamics from chronoamperometry is difficult because of the concordant onset of hydrogen evolution once minute seeds of Rh have formed. We observe the typical $j \sim t^{1/2}$ behaviour for the growth of deposits but overlaid with H_2 evolution which inhibits detailed analysis. A possible explanation for the different surface morphologies is the differences in the local current densities during Rh photoelectrodeposition: the smaller PS particle size leads to higher local current densities during electrodeposition through the smaller holes between the particles. This could lead to a shift from instantaneous to progressive nucleation of the Rh deposition and results in more numerous but smaller Rh nanoparticles formed within the rather short deposition time. The larger overall surface area of these deposits results in enhanced electrocatalytic activity.
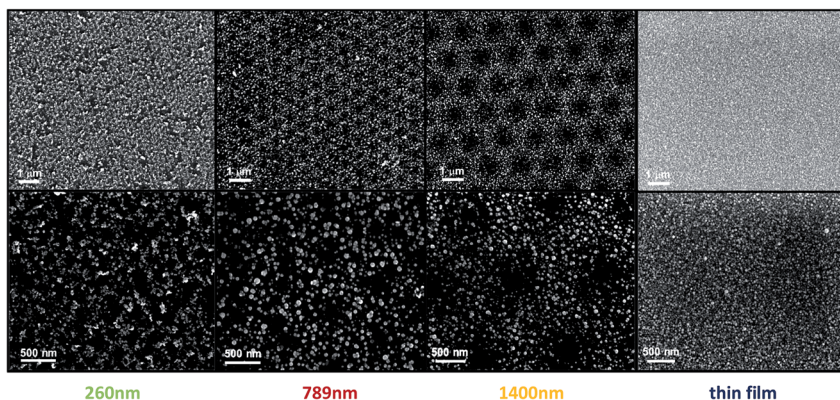

Fig. 5 HRSEM images of the nanostructured and thin-film p-InP–Rh photocathodes. The resolution is indicated with the scale bar in the images. The size of the applied polystyrene particle spheres onto the p-InP surface prior to Rh deposition is indicated below the images.

Table 1 Summary of Rh particle characteristics on the nanostructured and thin film photoelectrodes

	260 nm	789 nm	1400 nm	Thin film
Single Rh sphere diameter	~30 nm	~50–80 nm	~70–80 nm	~15–40 nm
Rh cluster size	0.002 μm² to 0.02 mm²	~0.008 μm²	~0.005 μm²	—
Rh particle coverage in cutout area (0.25 μm²)	32%	17%	24%	Full coverage

To characterize the surface chemistry of the nanostructured electrodes onto which 260 nm PS spheres were employed prior to the Rh deposition, X-ray photoelectron spectroscopy measurements (Fig. 6) were carried out. We compare the best performing system with the low performance one (Fig. 1b). Both samples show a clear signal from the InP substrate (Fig. 6b, c). The substrate signal from the thin film sample, however, is attenuated whereas the Rh signals are larger. Both samples show the $InPO_4$ signature (133.2 eV) from the HCl conditioning process (see experimental and methods[24,26]). The mean inelastic scattering length for photoelectrons in the observed binding energy range, λ_{esc}, lies in the range between 1–3 nm for Al K_α radiation and the different kinetic energies from the elemental core levels. The observation of a signal from InP for the thin film sample evidences that the Rh deposits are not fully covering the surface with a substantial number of pinholes present and that the interfacial film is at least partially thin enough to allow emission from the substrate. The
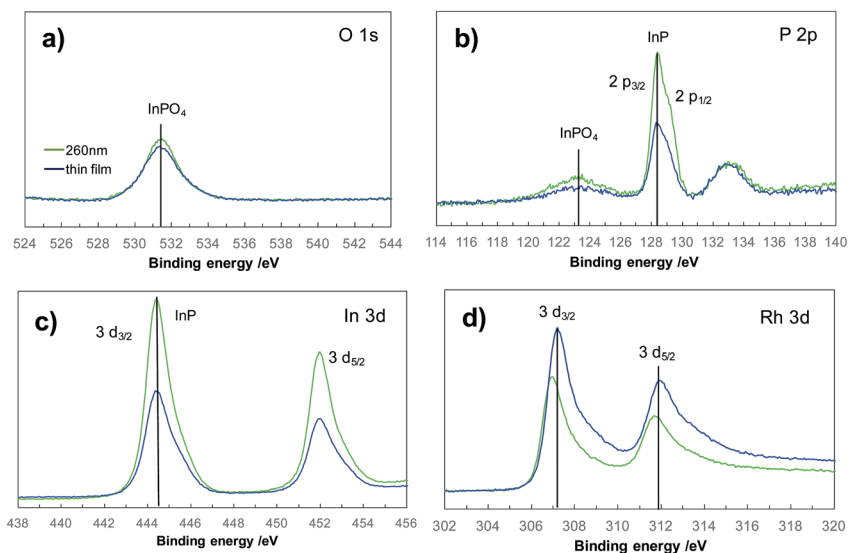

Fig. 6 X-ray photoelectron spectra of thin film and nanostructured photoelectrodes. (a) O 1s core level, (b) P 2p core levels, (c) In 3d core levels and (d) Rh 3d core levels. The legend in (a) indicates the colour code for the nanostructured (260 nm PS particle size) and thin film samples.
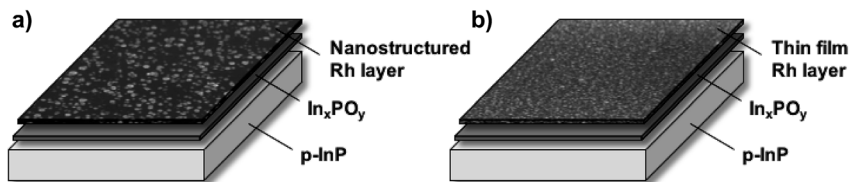
Fig. 7 Scheme of the (a) nanostructured and (b) thin film photoelectrodes and their compositions as suggested by using HRSEM and photoelectron spectroscopy.

overall Rh coverage, however, is larger than for the system prepared with 260 nm PS spheres as can be seen from the larger InP (128.4 eV) and the smaller Rh signal. The open areas for the PS-bead prepared structure show enhanced emission from InP where the InP surface is only covered by a thin layer of $InPO_4$. We presume a somewhat similar situation for the thin film sample, but with a considerably reduced area that is only covered by phosphate and not by Rh. This finding demands a further advance of our modeling, taking into account the topographic variations also for the thin film sample. In addition, the photocurrent data results show a substantial influence of interfacial electronics (including possibly energy band alignment). Fig. 7 summarizes the composition of the nanostructured (a) and thin film photoelectrodes (b) based on the X-ray photoelectron spectra and HRSEM.

The optical and surface topographical investigations suggest that the nano-structured photoelectrodes provide significant advantages over the thin film electrodes with respect to photoactivity and light transmission. In addition, the application of the smallest nanoparticle sphere size (260 nm) leads to a high coverage of small ($\sim$30 nm) Rh particles during Rh photoelectrodeposition, forming somewhat inhomogeneous clusters of different sizes on the p-InP surface (see Table 1). This particular structure features the highest light absorption among the nanostructured photoelectrodes, which goes along with the fact that these samples exhibited the best photoelectrochemical performance.

The here demonstrated application of SNL for advancing the hydrogen evolution reaction in semiconductor–electrocatalyst systems provides a model experiment for its further use in heterogeneous photoelectrocatalysis. Due to the possibility of systematically creating three-dimensional electrocatalyst nano-structures on photodiodes with well-defined optical properties, it serves as an interesting tool for the preparation of new electrocatalyst nanostructures for the production of solar fuels.

4 Conclusions

High activity rhodium electrocatalyst nanostructures have been prepared on p-InP by using shadow nanosphere lithography. We demonstrate that SNL allows direct deposition of the catalyst on photoactive semiconductors and that SNL can be used as a tool to specifically modify and design electrocatalyst structures. Our approach allows tuning of the optical and electronic properties of the electro-catalysts and therefore, altering the photoelectrocatalytic activity of the system.

Our findings indicate that the designed electrocatalyst nanostructures provide significant advantages for the photoelectrocatalytic half-cell performance by

improving the short-circuit current and achieving high photovoltages. Smaller polystyrene particle beads are generally favored, leading to a significant improvement of the photocurrent of the photodiode–electrocatalyst system. Optical and first electronic modelling of the various catalyst structures reproduces the trends observed experimentally and the data show that absorption and rather ideal Schottky junction assumptions have to be extended to further parameters involving recombination, transport in the complex structure, and energy band alignment, in this ongoing work. Overall, we demonstrate that shadow nanosphere lithography can be used as prosperous tool to precisely change the surface nano- and microtopography of the electrocatalyst on a light-absorbing semiconductor surface and therefore, establish new routes for the further development of efficient prototypes for then unassisted solar fuel generation.

Conflicts of interest

The authors declare no conflicts of interest.

Acknowledgements

References

1 J. Rongé, T. Bosserez, D. Martel, C. Nervi, L. Boarino, F. Taulelle, G. Decher, S. Bordiga and J. A. Martens, *Chem. Soc. Rev.*, 2014, **43**, 7963.

2 R. Sathre, C. D. Scown, W. R. Morrow III, J. C. Stevens, I. D. Sharp, J. W. Ager, K. Walczak, F. A. Houle and J. B. Greenblatt, *Energy Environ. Sci.*, 2014, **7**, 3264.

3 A. Fujishima and K. Honda, *Nature*, 1972, **238**, 37.

4 M. M. May, H. J. Lewerenz, D. Lackner, F. Dimroth and T. Hannappel, *Nat. Commun.*, 2015, **6**, 8286.

5 J. L. Young, M. A. Steiner, H. Döscher, R. M. France, J. A. Turner and T. G. Deutsch, *Nat. Energy*, 2017, **2**, 17028.

6 W. H. Cheng, M. H. Richter, M. M. May, J. Ohlmann, D. Lackner, F. Dimroth, T. Hannappel, H. A. Atwater and H. J. Lewerenz, ArXiv.org., 2017.

7 I. D. Sharp, J. K. Cooper, F. M. Toma and R. Buonsanti, *ACS Energy Lett.*, 2017, **2**, 139.

8 R. Gottesman and A. Zaban, *Acc. Chem. Res.*, 2016, **49**, 320.

9 K. T. Fountaine, H. J. Lewerenz and H. A. Atwater, *Appl. Phys. Lett.*, 2014, **105**, 173901.

10 H. J. Lewerenz, C. Heine, K. Skorupska, N. Szabo, T. Hannappel, T. Vo Dinh, S. A. Campbell, H. W. Klemm and A. G. Munõz, *Energy Environ. Sci.*, 2010, **3**, 748–760.

11 S. Hu, M. R. Shaner, R. Matthew, J. A. Beardslee, M. Lichterman, B. S. Brunschwig and N. S. Lewis, *Science*, 2014, **344**, 1005.

12 M. R. Shaner, M. T. McDowell, A. Pien, H. A. Atwater and N. S. Lewis, *J. Electrochem. Soc.*, 2016, **163**, H261.

13 O. K. Alexeeva and V. N. Fateev, *Int. J. Hydrogen Energy*, 2016, **41**, 3373.

14 D. Kong, H. Wang, Z. Lu and Y. Cui, *J. Am. Chem. Soc.*, 2014, **136**, 4897.

15 J. Grunes, J. Zhu, E. A. Anderson and G. A. Somorjai, *J. Phys. Chem. B*, 2002, **106**, 11463.

16 P. Patoka and M. Giersig, *J. Mater. Chem.*, 2011, **21**, 16783.

17 T. R. Jensen, M. D. Malinsky, C. L. Haynes and R. P. Van Duyne, *J. Phys. Chem. B*, 2000, **104**, 10549.

18 A. Kosiorek, W. Kandulski, P. Chudzinski and M. Giersig, *Nano Lett.*, 2004, **4**, 1359.

19 C. K. Dixit, A. Kumar and A. Kaushik, *Biochem. Biophys. Res. Commun.*, 2012, **423**, 473.

20 A. Heller and R. G. Vadimsky, *Phys. Rev. Lett.*, 1981, **46**, 1153.

21 Z. W. Seh, J. Kibsgaard, C. F. Dickens, I. Chorkendorff, J. K. Nørskov and T. F. Jaramillo, *Science*, 2017, **355**, eaad4998.

22 M. R. Shaner, K. T. Fountaine and H. J. Lewerenz, *Appl. Phys. Lett.*, 2013, **103**, 143905.

23 K. T. Fountaine, H. J. Lewerenz and H. A. Atwater, *Nat. Commun.*, 2016, **7**, 13706.

24 A. G. Muñoz, C. Heine, M. Lublow, H. W. Klemm, N. Szabó, T. Hannappel and H. J. Lewerenz, *ECS J. Solid State Sci. Technol.*, 2013, **2**, Q51.

25 J. C. Maxwell Garnett, *Philos. Trans. R. Soc. London*, 1904, **203**, 385.

26 A. G. Muñoz, C. Heine, T. Hannappel and H. J. Lewerenz, *Electrochim. Acta*, 2018, **260**, 861.